JOURNAL OF GEOPHYSICAL RESEARCH, VOL. 111, B12305, doi:10.1029/2006JB004415, 2006



# $M \geq 7.0$ earthquake recurrence on the San Andreas fault from a stress renewal model

Tom Parsons[1]

Received 28 March 2006; revised 24 July 2006; accepted 22 August 2006; published 19 December 2006.

[1] Forecasting $M \geq 7.0$ San Andreas fault earthquakes requires an assessment of their expected frequency. I used a three-dimensional finite element model of California to calculate volumetric static stress drops from scenario $M \geq 7.0$ earthquakes on three San Andreas fault sections. The ratio of stress drop to tectonic stressing rate derived from geodetic displacements yielded recovery times at points throughout the model volume. Under a renewal model, stress recovery times on ruptured fault planes can be a proxy for earthquake recurrence. I show curves of magnitude versus stress recovery time for three San Andreas fault sections. When stress recovery times were converted to expected $M \geq 7.0$ earthquake frequencies, they fit Gutenberg-Richter relationships well matched to observed regional rates of $M \leq 6.0$ earthquakes. Thus a stress-balanced model permits large earthquake Gutenberg-Richter behavior on an individual fault segment, though it does not require it. Modeled slip magnitudes and their expected frequencies were consistent with those observed at the Wrightwood paleoseismic site if strict time predictability does not apply to the San Andreas fault.

**Citation:** Parsons, T. (2006), $M \geq 7.0$ earthquake recurrence on the San Andreas fault from a stress renewal model, *J. Geophys. Res.*, *111*, B12305, doi:10.1029/2006JB004415.

## 1. Introduction

[2] Frequency of large earthquake occurrence forms the basis for seismic hazard assessments, and the concept of stress-driven earthquake renewal inspires time-dependent earthquake probability calculation. When empirical earthquake interevent times are lacking, hazard calculations are made with inferred values [e.g., *Working Group on California Earthquake Probabilities* (*WGCEP*), 2003]. Inference of recurrence rates can be approached using variants of the time-predictable model [*Shimazaki and Nakata*, 1980], where stress drop of the last earthquake divided by the long-term stressing rate yields the time to the next event. This concept has been applied by relating proxies such as earthquake slip and slip rate [*WGCEP*, 1995] or moment and moment rate [*WGCEP*, 2003], and where distributions of expected events are divided by rates to get recurrence statistics for probability calculations [*Savage*, 1992].

[3] A key question raised by *Shimazaki and Nakata* [1980] was whether earthquakes are time- or slip-predictable; that is, is the time of the next earthquake predictable from the slip of the past one, or is the slip of the next earthquake predictable from the slip of the past one? The key difference being that in time predictability, there is a stress threshold above which the fault always fails, whereas in slip predictability, there is a base stress state to which the fault always returns. An examination of the Parkfield segment of the San Andreas fault by *Murray and Segall* [2002] indicated behavior inconsistent with time predictability because of the long gap since the previous earthquake in 1966. The eventual 2004 $M$ = 6.0 earthquake was not consistent with slip predictability either, because the elapsed time since 1966 should have produced a larger ($M$ = 6.6–6.9 [*Murray and Segall*, 2002]) earthquake. Renewal as an effective forecast model was questioned altogether by *Kagan and Jackson* [1999], who noted large-earthquake clustering rather than periodicity. Paleoseismic data from the southern San Andreas fault is consistent with a combination of earthquake periodicity and clustering [*Weldon et al.*, 2004, 2005]. The position taken in this paper is recognition that earthquake hazard forecasts are derived from frequency estimates, and it is therefore worthwhile exploring the issue from stress-based perspective.

[4] The primary goal of this paper is to use methods and data independent of long-term geologic slip rate estimates to calculate earthquake recurrence. This should not be interpreted as a judgment on use of geologic slip rate data, but rather application of geodetic data to broaden the suite of San Andreas fault recurrence estimates. To make these calculations I used a finite element model of tectonic stressing rates derived from GPS observations [*Parsons*, 2006] to calculate the time required to recover stress drops from modeled scenario earthquakes centered on three major sections of the San Andreas fault. This method enabled calculations that affected a volume of crust and mantle and included postseismic viscoelastic relaxation effects.

## 2. Methods

[5] Large earthquake recurrence estimates and related tectonic stressing rates were calculated using finite element

[1]U.S. Geological Survey, Menlo Park, California, USA.

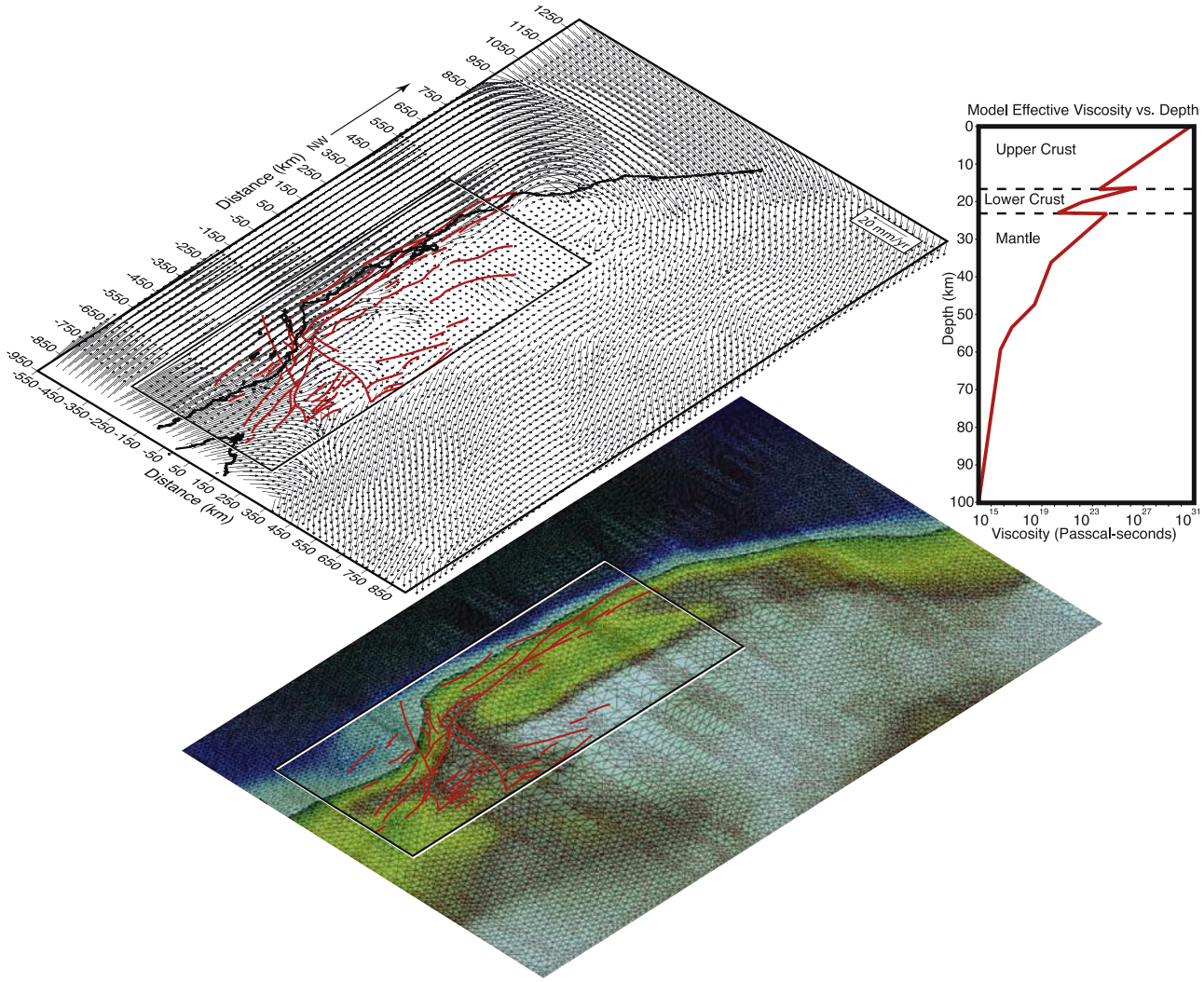


**Figure 1.** Three-dimensional model of the California lithosphere shown with the GPS-derived velocity field used to load the model superposed above. Red lines show major faults within the boxed study area. Large regions surrounding the study area were included to calculate boundary conditions. An example viscosity profile derived near the San Andreas fault is shown in the inset. Effective viscosity was calculated according to $n = \sigma^{1-n} \exp(Q_c / RT)/2A$, where $\sigma$ is differential stress (calculated with the finite element model), $R$ is the gas constant, and $Q_c$ (activation energy), $A$, and $n$ are experimentally determined constants (Table 1). Most of the strength in the model was carried in the crust because a partially wet upper mantle rheology was used.

analysis. Here I provide an overview of the finite element model, which is the same as employed by *Parsons* [2006]. A crustal and upper mantle structural model of California and surrounding tectonic provinces (Figure 1) was assembled using seismic velocity models, and rheological properties were derived from surface heat flow observations [*Parsons*, 2006]. Beneath a smoothed topographic surface, the model had defined upper and lower crustal layers of varying thickness that overlaid a ~100-km-thick uppermost mantle. The upper mantle layer thickness was set such that its base became hot and inviscid enough to not refer stress into the model from the bottom boundary conditions (freely slipping laterally, constrained vertically). The upper crust was assumed to have granitic material properties, the lower crust was associated with basaltic properties, and the upper mantle was defined by a mix of wet and dry dunite. Material constants are listed in Table 1.

[6] The model was composed of 136,447 elements defined by 212,016 nodes in a variable-sized mesh (average node spacing was 5 km) using viscoelastic tetrahedral elements. Meshing was conducted using higher-order three-dimensional (3-D) elements with quadratic displacement behavior best suited to modeling irregular meshes. Elements were defined by 10 nodes, each having three degrees of freedom (translations in the nodal x, y, and z directions). All elements in this study had capability of elastic and inelastic deformation, with inelastic strain behavior defined by a rate-dependent creep relation. This choice was made because postseismic and other transient geodetic observations are well matched with models using

**Table 1.** Material Constants Used in the Three Layers of the Finite Element Model[a]

| Parameter | Upper Crust Layer | Source | Lower Crust Layer | Source | Upper Mantle | Source |
|---|---|---|---|---|---|---|
| $E$, Young's modulus, MPa | $8 \times 10^4$ | 1 | $9 \times 10^4$ | 1 | $1.9 \times 10^5$ | 1 |
| $A$, physical constant, MPa$^{-n}$ s$^{-1}$ | $2.0 \times 10^4$ | 2 | $6.3 \times 10^{-2}$ | 5 | $5.0 \times 10^3$ | 6 |
| $n$, physical constant | 1.9 | 2 | 3.1 | 5 | 3.8 | 6 |
| $Q_c$ activation energy, kJ mol$^{-1}$ | 140.6 | 2 | 276 | 5 | 492 | 6 |
| $\nu$, Poisson's ratio | 0.25 | 3 | 0.26 | 3 | 0.28 | 3 |
| $\rho$, density, kg m$^{-3}$ | $2.7 \times 10^3$ | 4 | $2.8 \times 10^3$ | 4 | $3.0 \times 10^3$ | 4 |

[a]Elements in the model are all viscoelastic, with rate-dependent creep behavior controlled by the temperature gradient and the listed constants. References: 1, *Birch* [1966]; 2, *Hansen and Carter* [1983]; 3, *Christensen* [1996]; 4, *Christensen and Mooney*, [1995]; 5, *Caristan* [1982]; 6, *Carter and Tsenn* [1987].

power law descriptions of lithospheric rheology [e.g., *Pollitz et al.*, 2000; *Freed and Bürgmann*, 2004] and because it enabled a gradual transition from primarily elastic behavior into viscoelastic with increasing depth. Time-independent elastic strain ($\varepsilon$) occurred in the model according to

$$\varepsilon = \frac{\sigma}{E}, \tag{1}$$

where $E$ is Young's modulus and $\sigma$ is differential stress. Modeled time-dependent inelastic strain rate ($\dot{\varepsilon}$) was controlled by the creep equation [e.g., *Kirby and Kronenberg*, 1987]

$$\dot{\varepsilon} = A \exp(-Q_c/RT)\sigma^n, \tag{2}$$

where $A$, $Q_c$ (activation energy), and $n$ are experimentally derived constants, $R$ is the universal gas constant, and $T$ is temperature. Equation (2) added an increasingly important contribution to modeled strain with increasing temperature. Thus the model did not have specified viscosity in each layer; instead flow was controlled by the geothermal gradient and was influenced by material properties [*Parsons*, 2006].

[7] The model was defined with major strike-slip faults included. These were defined by cuts through the model crust that were faced with zero thickness contact elements obeying a Coulomb friction criterion. During stressing rate calculations, known creeping faults were allowed to slip with a uniform friction coefficient $\mu = 0.2$ because of their impact on crustal stress distribution. During earthquake simulations, all faults were kept locked except the rupturing segment and the deeper parts of the faults beneath the ruptures, which were permitted to have frictional postseismic afterslip.

### 2.1. Stressing Rate Calculations

[8] Tectonic stressing rates are an essential component in calculating earthquake recurrence via stress recovery time. In a renewal model, stress in the crust results from elastic strain accumulation caused by continuous plate motions. If strain from relative plate motion was constant across the boundary between the Pacific plate and the Sierra Nevada block, then the tectonic stressing rate would be a uniform gradient across the San Andreas fault zone. However, within times intervening between large earthquakes, it appears from geodetic observations and geometric considerations [*Li and Liu*, 2006] that crustal strain is nonuniform (Figure 1). Thus the California finite element model was loaded with an extrapolated and interpolated strain field derived from GPS observations, while boundary condition areas were moved at plate rates; crustal stressing rates were then derived from the input displacements [*Parsons*, 2006].

[9] Calculations using geodetic velocities defined a ~200-km-wide zone of relatively higher crustal stressing rates across the San Andreas fault system (Figure 2). The 25-km spaced grid of defined velocities in the input loads (Figure 1) caused a broader loading field than was calculated with a deep dislocation stressing model [*Smith and*

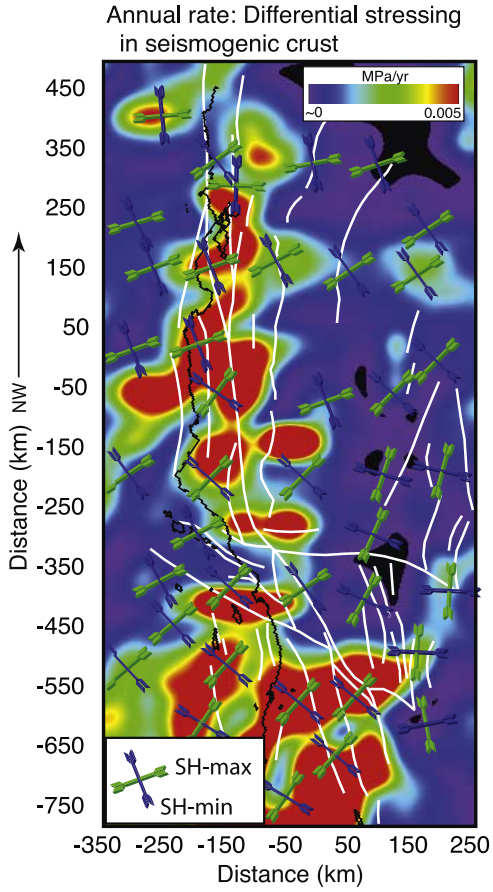


**Figure 2.** Contour plot of differential stressing rate (difference between greatest and least principal stresses) in the seismogenic crust from *Parsons* [2006]. Stressing rates were calculated with the finite element model and GPS velocity grid shown in Figure 1 and were used to calculate stress recovery times from modeled scenario earthquakes. Green and blue arrows show calculated orientations of maximum and minimum horizontal stresses, respectively.

*Sandwell*, 2003]. Surface deformation can be reproduced either with deep dislocation slip or with distributed loading [e.g., *Lisowski et al.*, 1991; *Savage et al.*, 1999; *Smith and Sandwell*, 2006], meaning that the actual driving mechanism remains an open question and a source of uncertainty in stressing rate calculations.

### 2.2. Earthquake Simulations

[10] Under any renewal model, earthquakes are expected to release stress from the crust. Earthquake simulations using elastic dislocations and Coulomb stress calculations imply that a volume of lithosphere is affected, as evidenced by earthquake rate decreases [e.g., *Harris and Simpson*, 1996, 1998; *Stein*, 1999], though questions persist as to the strength of the evidence [*Felzer and Brodsky*, 2005]. In this study, a volumetric approach was taken both in stressing rate and stress drop calculations. This enabled inclusion of stress transfer concepts such as deep fault afterslip and viscoelastic relaxation of the mantle [*Nur and Mavko*, 1974; *Savage and Prescott*, 1978; *Freed and Lin*, 1998; *Kenner and Segall*, 1999; *Nostro et al.*, 2001; *Pollitz*, 2001; *Bürgmann et al.*, 2002; *Hearn et al.*, 2002; *Michael*, 2005].

[11] Scenario earthquake ruptures of varying magnitude were developed along three major San Andreas fault sections that I refer to as south, central, and north (Figures 3–10). Coseismic ruptures were confined to the upper crustal layer in the model, which was defined as the part of the crust having seismic velocity $\leq$6.5 km $s^{-1}$, and which varied in depth along the San Andreas fault trace [*Parsons*, 2006]. Magnitudes were defined using a magnitude-area relationship derived for strike-slip earthquakes with rupture area ($A$) greater than 500 $km^2$ [*Ellsworth*, 2003] where

$$M = 3.1 + (4/3)\log_{10}(A). \quad (3)$$

[12] Mean fault displacements in m ($S$) were calculated from a regression of *Wells and Coppersmith* [1994] for strike-slip faults as

$$\log_{10}(S) = -6.32 + 0.90M. \quad (4)$$

[13] Earthquakes were simulated by displacing nodes on both sides of the San Andreas fault each by half the mean displacement over the fault area corresponding to a given magnitude. Finite element static stress change calculations are equivalent to those from boundary element elastic dislocation calculation methods [*Parsons*, 2002].

[14] Coseismic static stress drops were calculated at every model node from scenario earthquakes on three San Andreas fault sections for a magnitude range between $M$ = 7.0 and $M$ = 8.0. Coseismic stresses are expected to increase and decrease in different crustal volumes [e.g., *Stein*, 1999]; in this study I only considered points with calculated stress drop and did not allow for earthquake interactions. For strike-slip ruptures, calculated stress changes are mostly negative except for near rupture terminations [e.g., *Harris and Simpson*, 1996, 1998; *Stein et al.*, 1997]. The case not considered here is a rupture initiating at the termination of a previous strike-slip earthquake that has a shortened recurrence time from stress increases; this instance is the subject of long-term fault evolution models [e.g., *Smith and Sandwell*, 2006].

[15] The finite element model was subjected to gravity, which enabled calculation of the full stress tensor at every point resulting from the overburden pressure, and changes in tensor components caused by fault slip. The stress tensor was resolved into principal stresses, allowing all stress changes and stressing rates to be expressed as changes in differential stress, defined as the difference between the greatest and least principal stresses. Differential stress drives faulting [*Anderson*, 1951], and unlike Coulomb stress changes, can be defined at points irrespective of a particular fault plane or predefined regional stress direction. Stress recovery times were calculated by dividing coseismic and postseismic differential stress drops at each model node by the differential stressing rate calculated by *Parsons* [2006] for that node. If earthquake recurrence is inferred from recovery times calculated this way, then the implication is that recurrence requires complete regeneration of stresses lost in the previous earthquake. A Coulomb model differs in that it is dependent on fault friction; therefore calculated recurrence in a Coulomb model might be advanced or delayed relative to the differential stress method depending on estimated fault strength.

[16] Postseismic effects were also tracked in the model by allowing 100 years of deformation to occur after the simulated earthquakes through afterslip on the fault beneath the coseismic rupture and lower crustal and upper mantle flow. These processes tended to recharge stresses back into the crust and onto the coseismic rupture plane, shortening recurrence times (discussed in Section 3). In summary, calculated recovery time at a given point in the model volume was a function of the sum of coseismic and postseismic stress change magnitude, and spatially varying differential stressing rates.

## 3. Results

[17] I calculated stress recovery times within a three-dimensional model of the California crust for a range of $M \geq 7.0$ scenario earthquakes. The results of these calculations on three San Andreas fault sections were contoured in years and are shown in Figures 3, 7, and 9. Longer recovery times were calculated at points with the largest stress drops, such as on and near rupture surfaces (Figure 3), and where stressing rates were calculated to be lowest (Figure 2). Stress recovery times in the affected volumes surrounding the ruptures can be thought of as durations of expected stress shadows cast by scenario earthquakes.

[18] Slip of scenario earthquakes was constant at the mean determined from equation (4); therefore disparity in recovery time along fault strike resulted primarily from variation in calculated differential stressing rate (Figure 2). This effect can be seen readily in Figure 7, where parts of the ruptured San Andreas fault model show longer recovery times than others. This is one consequence of the stressing rate model used, which is that fault sections with low differential stressing rates could act as barriers that inhibit earthquake slip. Modeled stressing rate variations resulted from observed variation in crustal strain [*Parsons*, 2006]; to the degree that they reflect real Earth processes, they might be assessed for consistency with fault segmentation models.

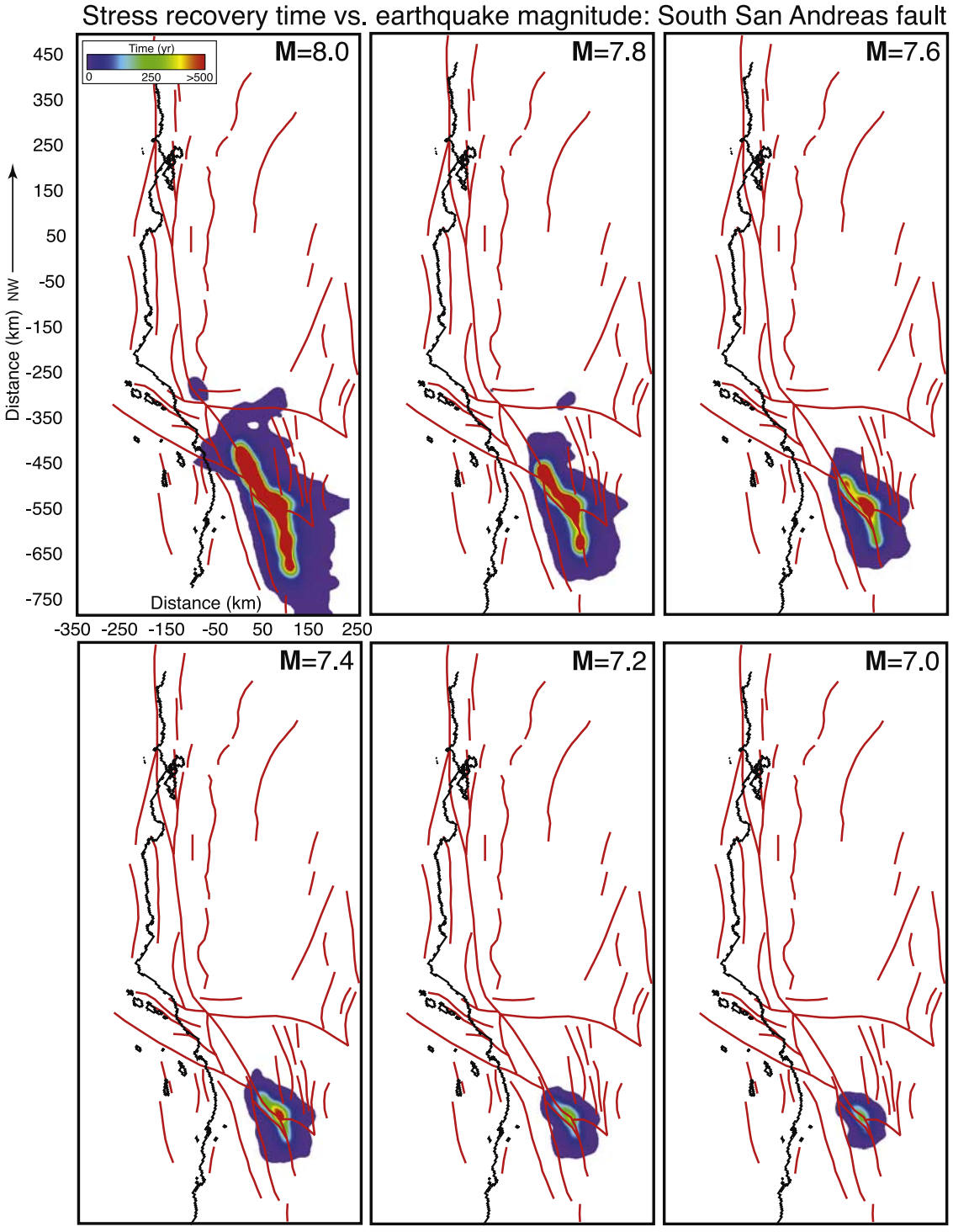


**Figure 3.** Map view contours of stress recovery time in years for $M$ = 7.0 to $M$ = 8.0 earthquakes centered on the southern San Andreas fault. Times were found by dividing the calculated differential static stress drop by calculated stressing rate at each model node. Under a stress renewal model, times shown on the fault rupture can be thought of as recurrence interval, while off-fault times can be thought of as stress shadow duration. Simulated earthquake rupture areas were related to magnitude using equation (3), while slip was scaled using equation (4). Dependence of the lithospheric volume affected on earthquake magnitude can be assessed by areal differences in mapped recovery times.

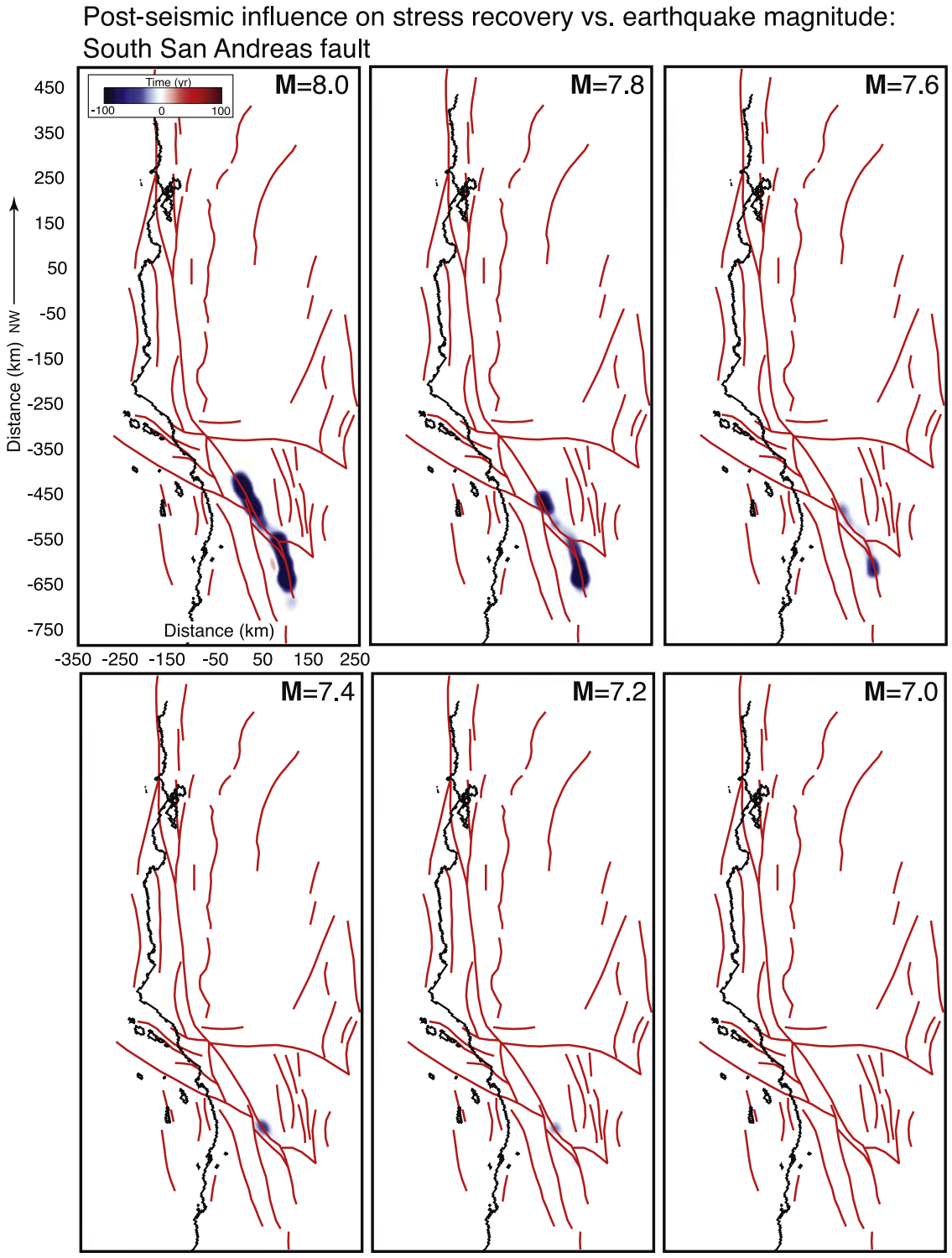


**Figure 4.** Contoured (in years) contribution of postseismic afterslip and viscoelastic relaxation on stress recovery times shown in Figure 3 for the southern San Andreas fault. The dominant effect is shortening recovery times (blue colors) because of postseismic stress transfer back into the crust. In the model, postseismic effects are most significant for $M \geq 7.6$ earthquakes and are negligible for $M \leq 7.4$ events.

[19] Stress recovery times depicted in Figures 3, 7, and 9 include modeled stress recharge from postseismic relaxation and afterslip beneath the simulated earthquakes. In all cases, postseismic relaxation acted to reduce the stress recovery time in the model crust, mostly concentrated on and near the San Andreas fault (Figures 4, 8, and 10). For the largest scenario earthquakes ($M \geq 7.6$), postseismic effects shortened stress recovery times in excess of 100 years, which

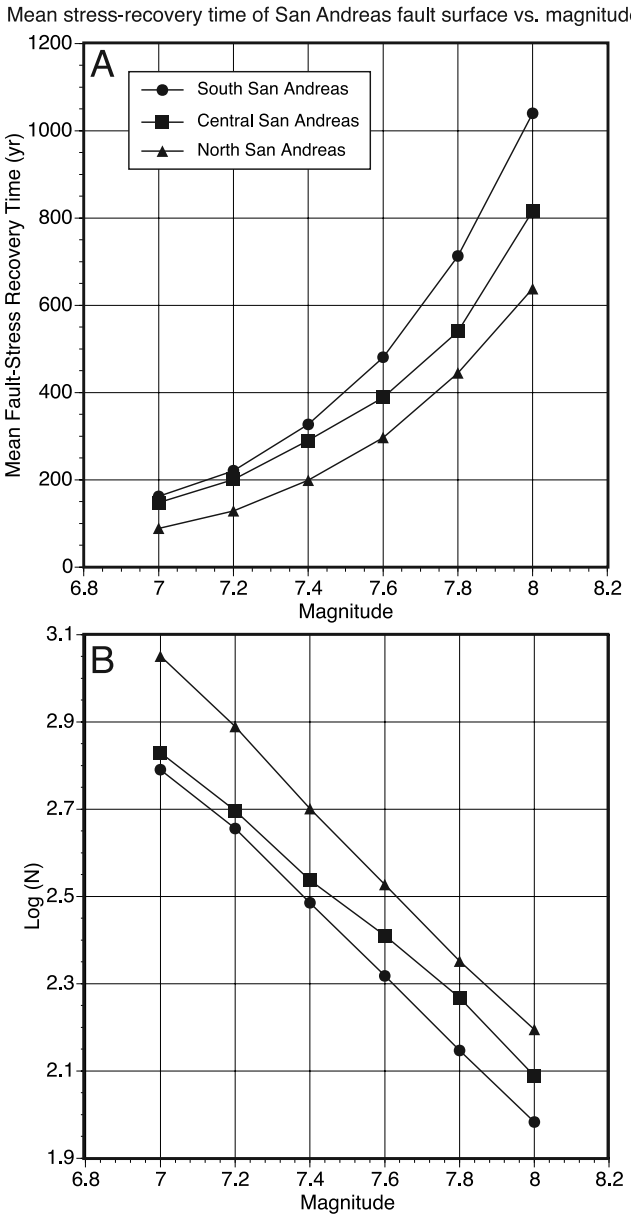


**Figure 5.** (a) Plots of mean stress recovery times averaged on the ruptured San Andreas fault surface vs. model earthquake magnitude on three fault sections (see Figures 3, 7, and 9 for locations). Under a renewal model, fault surface stress recovery times can be thought of as earthquake recurrence times. (b) Same information as in Figure 5a except stress recovery times are expressed as the logarithm of event frequencies in a hypothetical 10 kyr period. The distribution is linear as in a Gutenberg-Richter relationship.

could be up to a ~25% reduction (Figure 5). Postseismic effects were calculated as having a negligible effect on stress recovery times of scenario earthquakes of $M \leq 7.4$ (Figures 4, 8, and 10). The magnitude of modeled postseismic relaxation loading in the crust was highly dependent on rheological parameters, which in this study were extrapolated from surface heat flow [*Parsons*, 2006] and from physical constants used in equation (2) (Table 1). Postseismic relaxation and afterslip acting to recharge stress and shorten modeled earthquake recurrence is consistent with other theoretical and modeling studies [*Nur and Mavko*, 1974; *Savage and Prescott*, 1978; *Freed and Lin*, 1998; *Kenner and Segall*, 1999; *Nostro et al.*, 2001; *Pollitz*, 2001; *Bürgmann et al.*, 2002; *Hearn et al.*, 2002; *Michael*, 2005]. While this may lend confidence in the sign of the results shown in Figures 4, 8, and 10, the magnitude of the effect has to be considered model-dependent.

### 3.1. Stress Recovery as a Proxy for Earthquake Recurrence

[20] If earthquakes are time-predictable, then the stress drop of the last earthquake divided by the stressing rate yields the time until the next event [*Shimazaki and Nakata*, 1980]. Under that assumption, stress recovery times mapped in Figures 3, 7, and 9 were used to calculate $M \geq 7.0$ earthquake recurrence times by averaging values at the San Andreas fault surface (Figure 5a). Stress-based recurrence times were calculated to be shortest for the smallest earthquakes considered ($M = 7.0$), and to grow nonlinearly with increasing magnitude (Figure 5). If the investigated San Andreas fault sections could produce the full range of modeled $M = 7.0$ to $M = 8.0$ earthquakes, then recurrence times could be expressed as the logarithm of expected event frequencies and plotted against magnitude (Figure 5b). Frequency-magnitude plots from modeled $M \geq 7.0$ earthquakes defined a linear trend as in a Gutenberg-Richter relationship (Figure 5b). A stress-balanced model of the San Andreas fault is consistent with either repeated characteristic earthquakes or distributed magnitudes according to a Gutenberg-Richter model. However, a characteristic earthquake stress balance model would not fit the curves shown in Figures 5 and 6, and instead would deviate at the higher magnitude range.

[21] Calculated recurrence vs. magnitude distributions were fit to Gutenberg-Richter models with a b value (slope) of 0.87 for the north San Andreas fault example, 0.73 for the central section, and 0.82 for the southern section (Figure 5b). It is convenient to discuss stress-based recurrence results on a Gutenberg-Richter trend because it readily demonstrates model implications on magnitude distribution and overall earthquake rates. In the model, b values less than 1.0 resulted from increasing contribution of postseismic effects that preferentially shortened the largest earthquake stress recovery times as compared with smaller ruptures (Figures 4, 8, and 10).

[22] The Gutenberg-Richter plots of Figure 5b show regional differences in the a value (intercept), or overall expected earthquake rate. Characteristics of regional magnitude-frequency distributions inferred from calculated recurrence times in Figure 5a were a function of three spatial effects: the calculated distribution of differential stress change at different locations, spatial variations in calculated stressing rates, and differing contributions of postseismic relaxation. Scenario earthquake magnitudes were determined from the area relationship of equation (3). Seismogenic depth in the model was variable, tending to be deeper in the thickened crust in the central San Andreas example than to the north or south. Thus slip was distributed a little differently with depth, depending on location, leading to slightly different distributions of coseismic stress change. The effects of stressing rate can be seen clearly

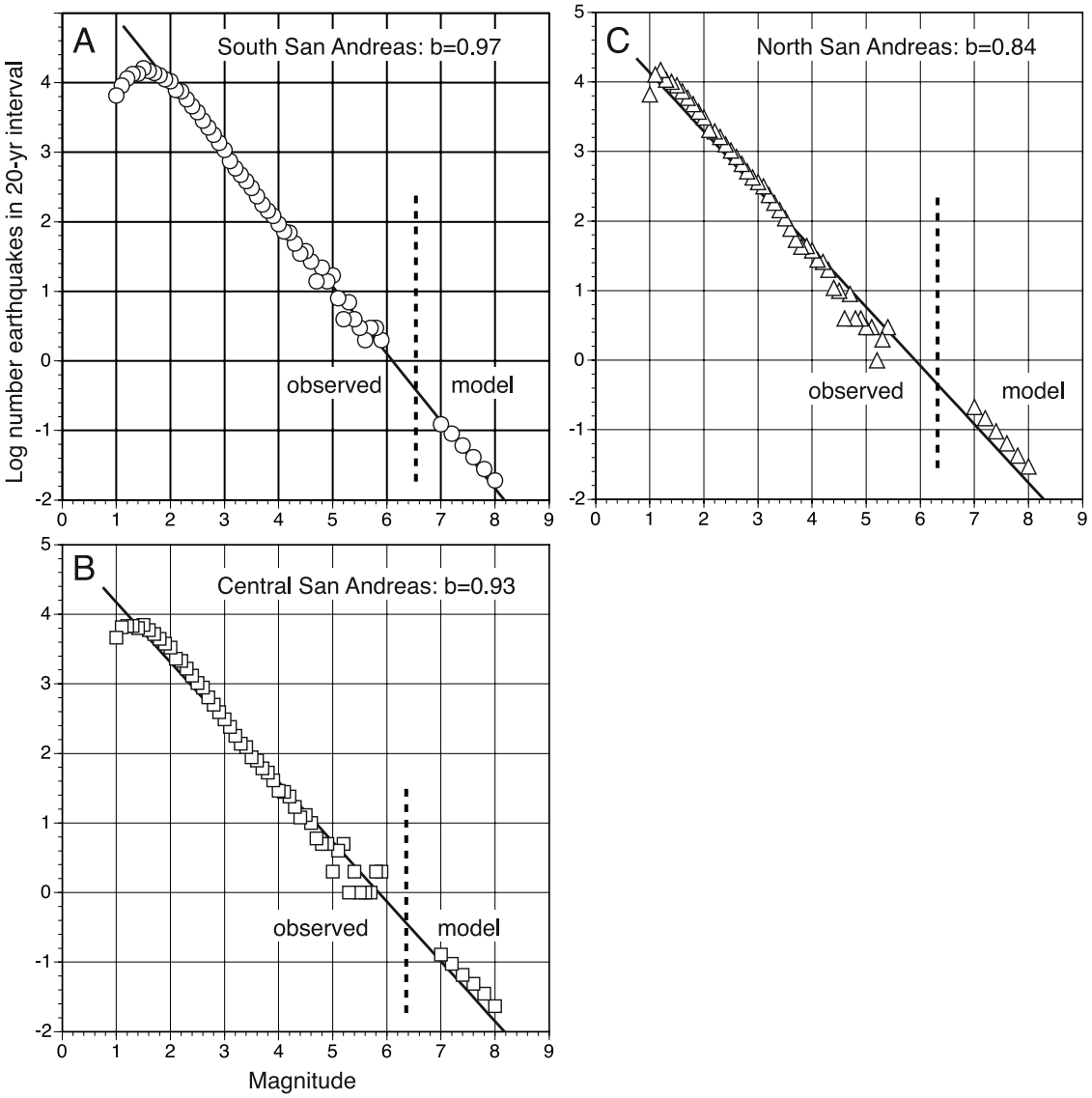


**Figure 6.** Comparison of observed magnitude-frequency distributions from 20 years of $M \leq 6.0$ earthquakes from the (a) southern, (b) central, and (c) north regions (see Figures 3, 7, and 9 for locations) with the calculated magnitude-frequency distributions from Figure 5b normalized for a 20-year period. Rates calculated from the stress recovery model are in reasonable agreement with expected rates from the observed seismicity.

when comparing the north and south San Andreas stress recovery versus magnitude curves. Stressing rates were calculated to be low along a significant part of the south San Andreas fault, possibly because of post-Landers earthquake transients in the GPS signal used to load the model [*Parsons*, 2006] (Figure 2). In addition, calculated positive stressing rates were more broadly distributed across the southern part of the California model than the north, yielding longer stress recovery times.

[23] I compared modeled magnitude-frequency distributions of $M \geq 7.0$ earthquakes with observed relationships calculated from $M \leq 6.0$ earthquakes in the three regions. Observed Gutenberg-Richter curves were calculated with a least squares method from 20 years of seismicity taken from areas around the San Andreas fault corresponding to the volumes affected by $M = 8.0$ ruptures in Figures 4, 7, and 9. Observed frequency-magnitude relations were then compared to the rate plots of Figure 5b normalized to 20 years (Figure 6). Modeled rates of large earthquakes could be fit to observed with some modification to the b values: the southern San Andreas b value changed from 0.82 to 0.97 (standard deviation = 0.06), the central section from 0.73 to 0.93 (standard deviation = 0.09), and the northern section remained about the same (0.87 to 0.84; standard deviation = 0.09). The San Andreas fault represents the primary source of $M \geq 7.0$ earthquakes in the three regions where b values were calculated, thus the fit between modeled large earthquakes and observed smaller shocks was not unexpected. To summarize, the array of calculated large earthquake recurrence rates using a stress recovery model show Gutenberg-Richter behavior that is consistent with observed rates of smaller earthquakes in regions corresponding to the simu-

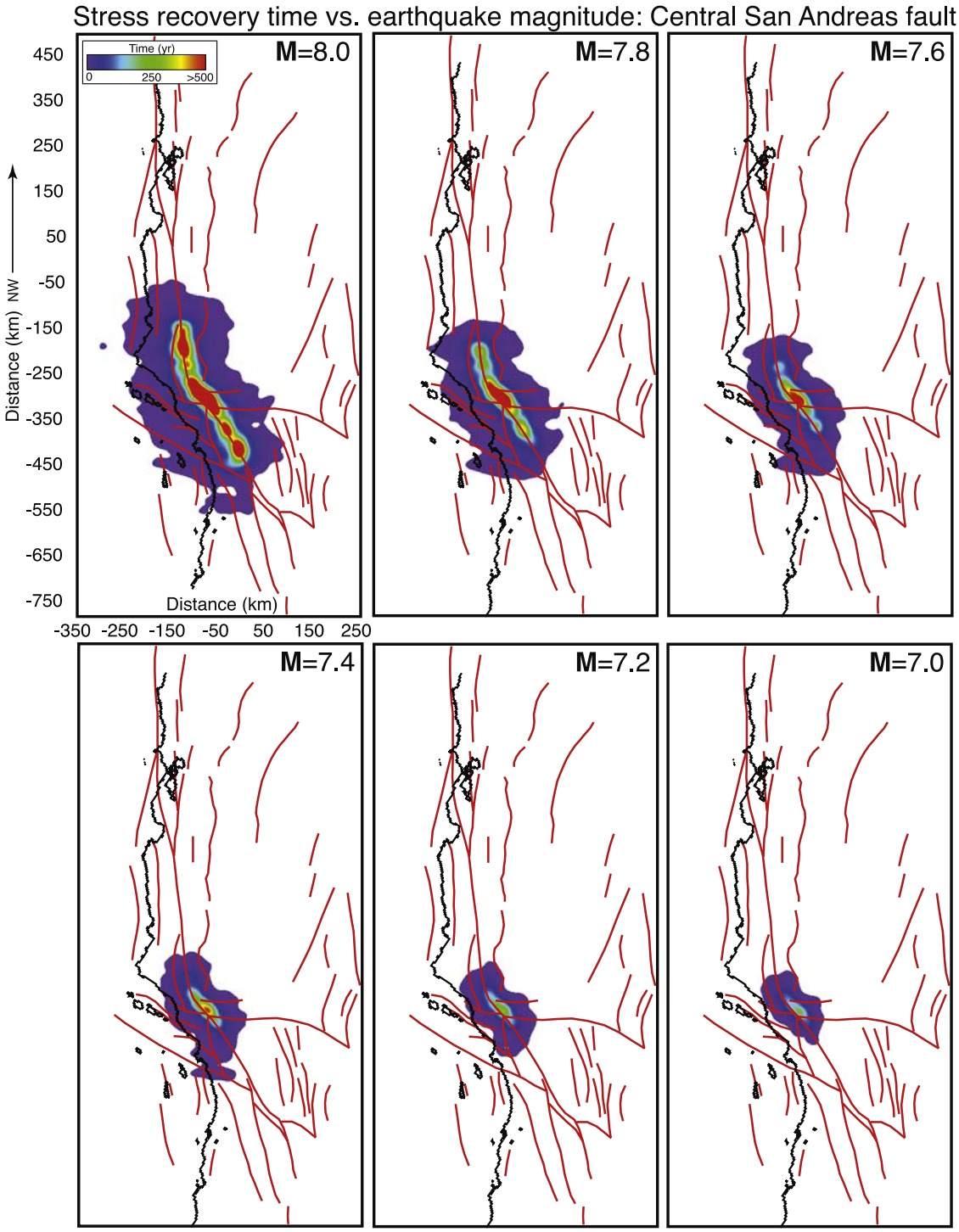


**Figure 7.** Map view contours of stress recovery times in years for $M$ = 7.0 to $M$ = 8.0 earthquakes centered on the central San Andreas fault. Same as Figure 3 except for the locations of the simulated earthquakes.

lations. Gutenberg-Richter behavior is not a model requirement because stress could be balanced with repeating characteristic earthquakes of the same size.

### 3.2. Comparison of Modeled Earthquake Frequency to Observed San Andreas Fault Offsets

[24] Here I compare modeled earthquake frequency with paleoseismic observations made at the Wrightwood site on the southern San Andreas fault by *Weldon et al.* [2004]. The Wrightwood site has a complete record of earthquake displacements for the past 1500 years. Slip observations were binned by displacement magnitude (1-m bins stepped by 0.5-m intervals) and plotted by their mean interevent times (Figure 11a). In Figure 11a model earthquake slip is plotted against calculated recurrence times from the southern and central San Andreas simulations, both of

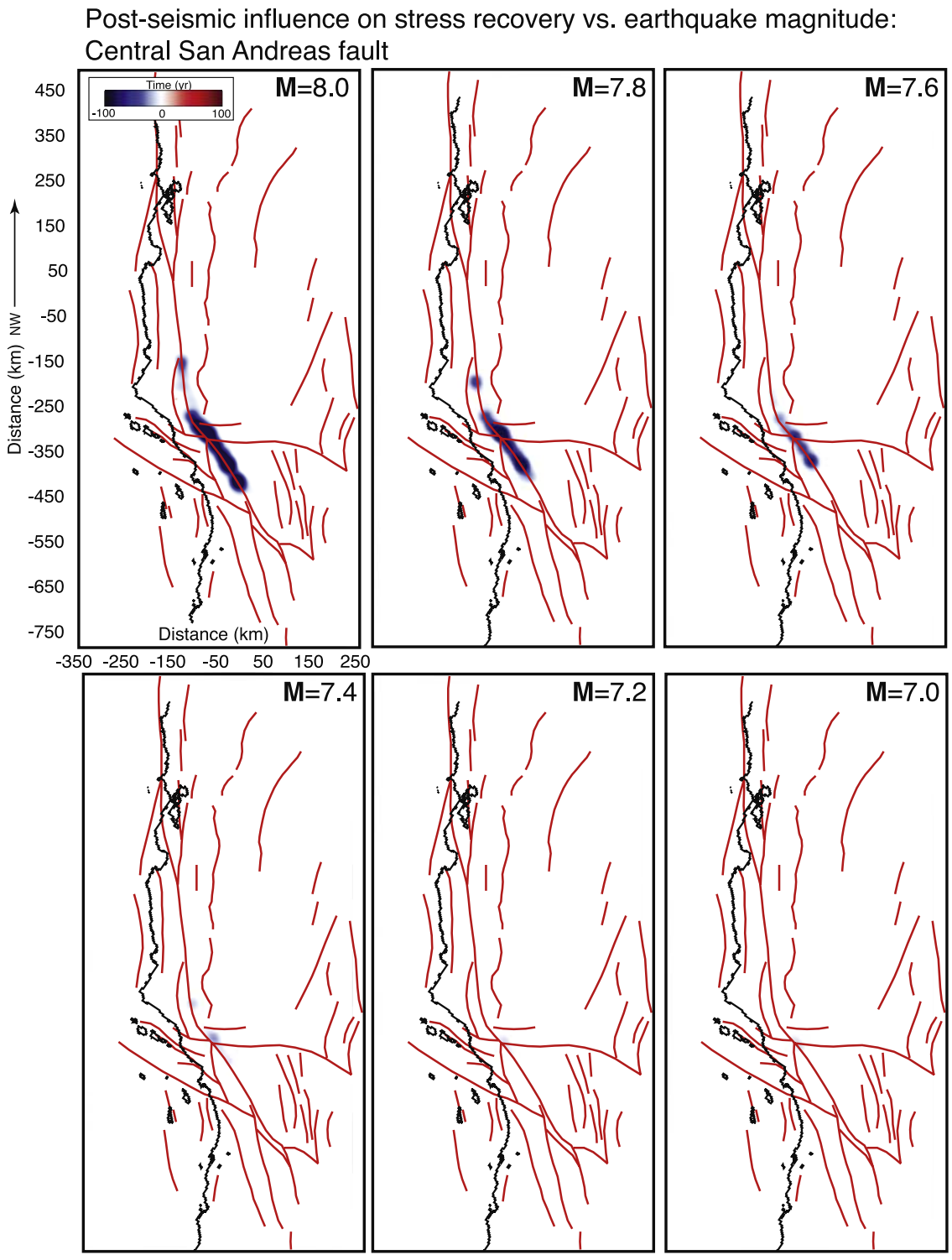


**Figure 8.** Contoured (in years) contribution of postseismic afterslip and viscoelastic relaxation on stress recovery times shown in Figure 7 for the central San Andreas fault. Same as Figure 4 except for the locations of the simulated earthquakes.

which overlap the Wrightwood site. In the observed and modeled cases, there is a linear trend of increased interevent time as a function of displacement that is in reasonable agreement, though the number of the largest slip events is necessarily small.

[25] *Weldon et al.* [2004] demonstrated that the Wrightwood data are neither slip- nor time-predictable, with the possible exception of the largest slip events. That is, taken in sequence, Wrightwood slip events showed little influence from the preceding slip magnitude (Figure 11b). Overlapping ruptures (Figure 11c) might explain some but not all of

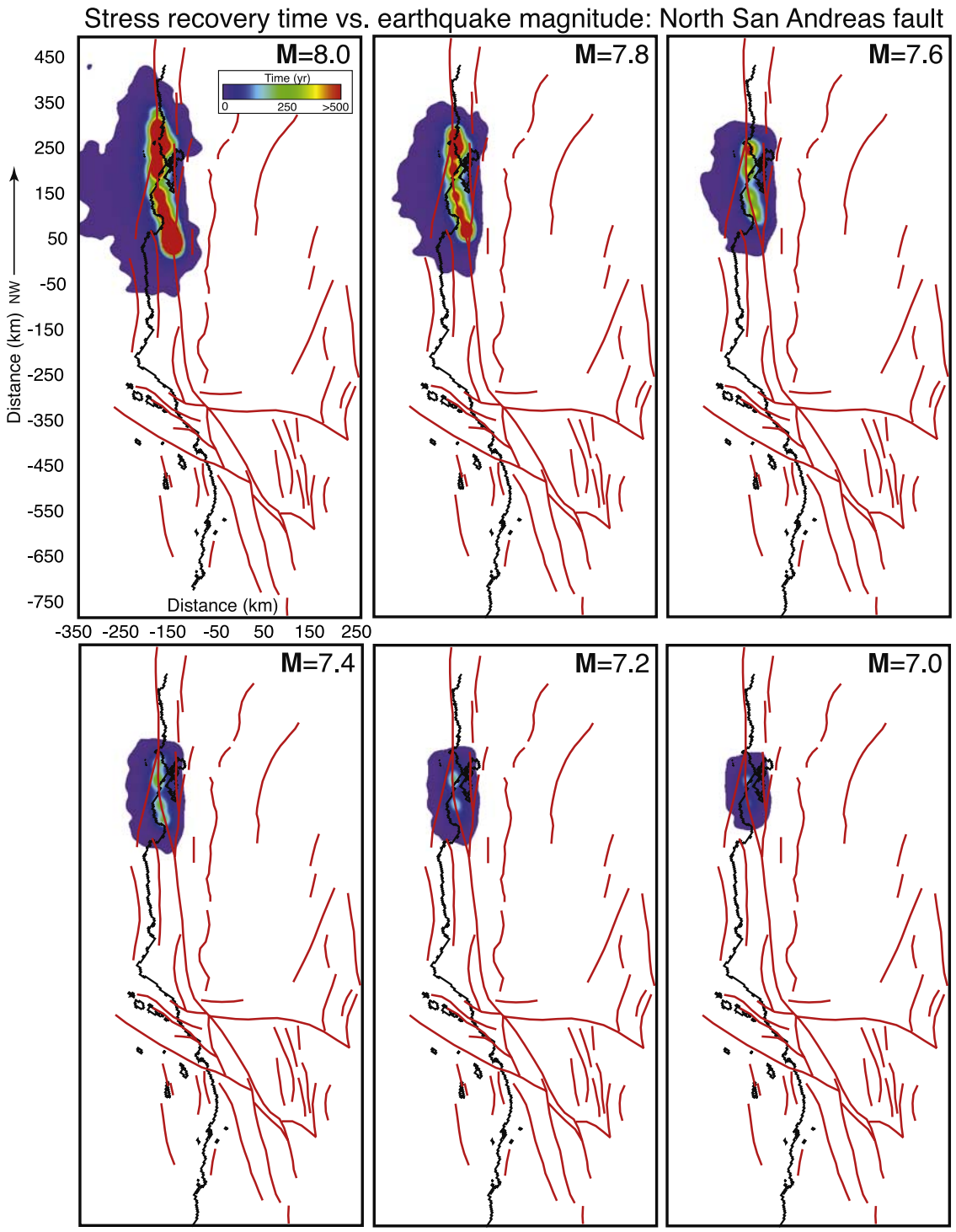


**Figure 9.** Map view contours of stress recovery times in years for $M$ = 7.0 to $M$ = 8.0 earthquakes centered on the northern San Andreas fault. Same as Figures 3 and 7 except for the locations of the simulated earthquakes.

the irregularity as was determined from analysis of nearby San Andreas sites [*Weldon et al.*, 2005]. One explanation for the Wrightwood series is that there is enough stress on the fault to sustain clustered large earthquakes, and that it is not necessary for the full stress recovery time to elapse between events. However, when the Wrightwood displacements are binned by slip magnitude, there is a rough periodicity to the observations, with largest events expected less frequently (Figure 11a). Correspondence between observed periodicity and calculated stress-based periodicity implies that there is increasing delay for stress recharge after the largest earthquakes. To summarize, mean slip in simulated earthquakes and calculated time required to recover

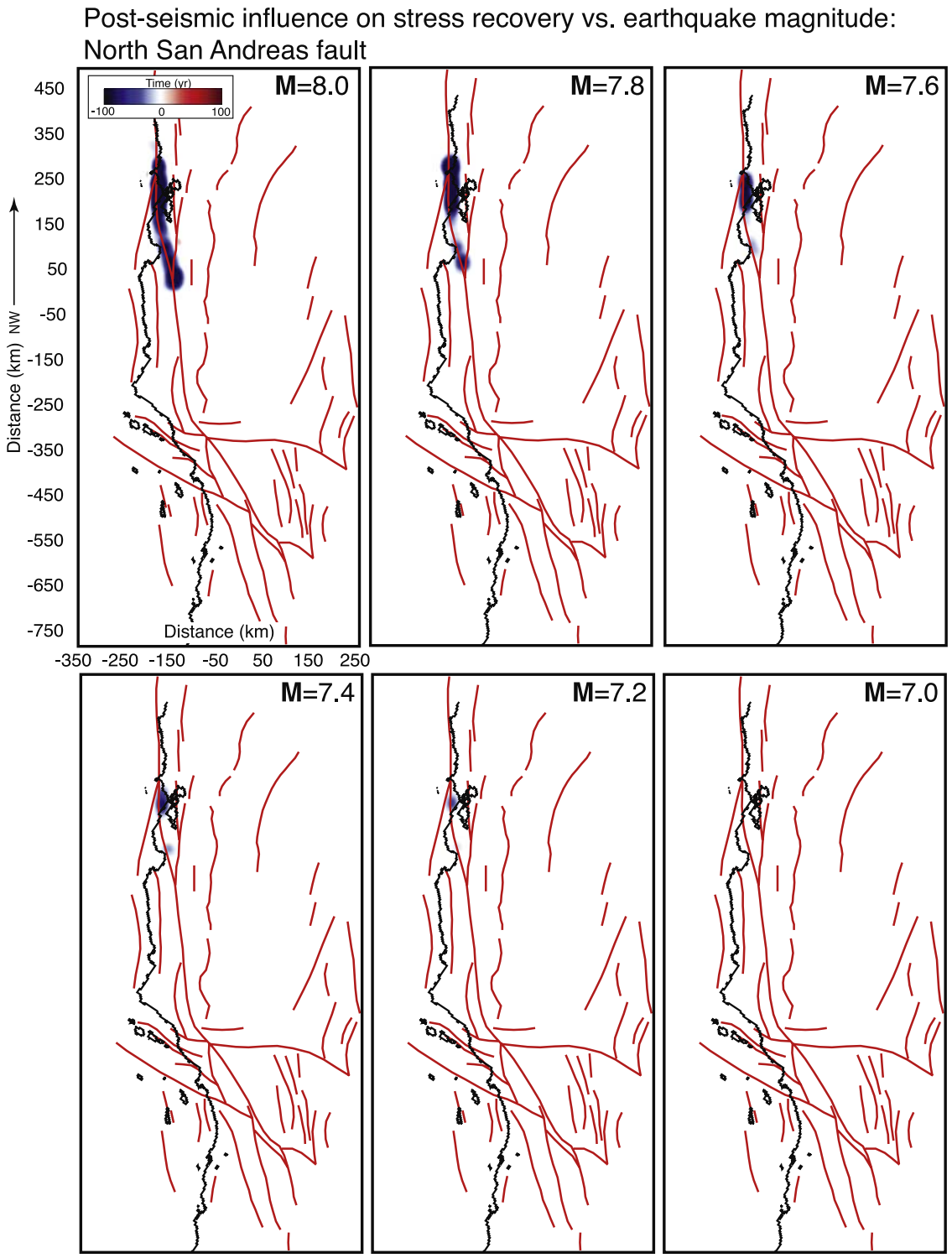


**Figure 10.** Contoured (in years) contribution of postseismic afterslip and viscoelastic relaxation on stress recovery times shown in Figure 9 for the northern San Andreas fault. Same as Figures 4 and 8 except for the locations of the simulated earthquakes.

stress drop is consistent with observed mean recurrence of comparable slip events at the Wrightwood site.

### 3.3. Hazard Implications

[26] Time-dependent earthquake probability calculations are made by integrating a recurrence model over the time elapsed since the last earthquake on a given fault section. Time-independent calculations use an exponential or Poisson distribution of a given mean. This paper presents stress-based recurrence time calculations for an array of $M \geq 7.0$ San Andreas ruptures. Modeled interevent times are consistent with observations at Wrightwood only when consider-

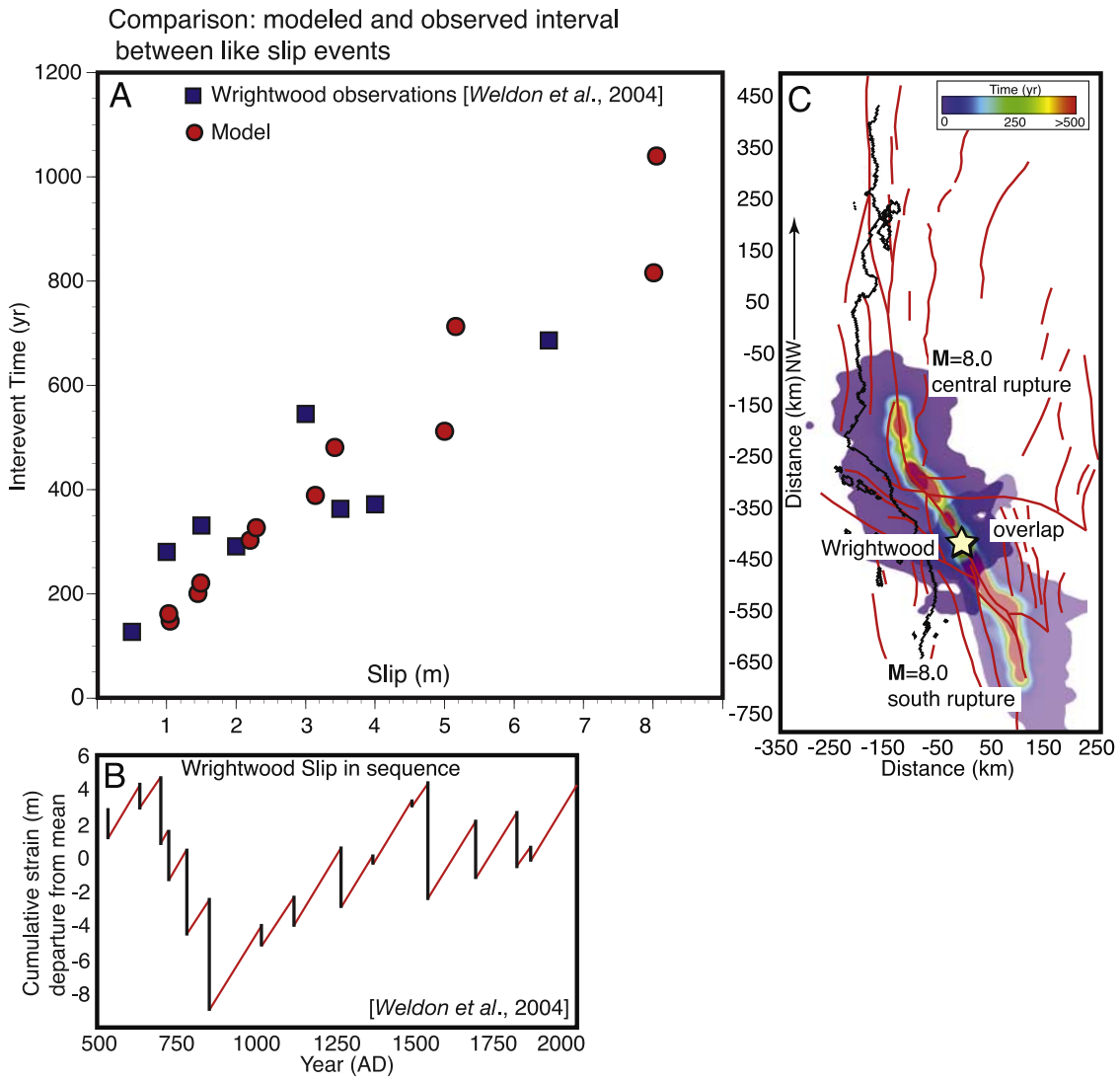


**Figure 11.** (a) Comparison of modeled earthquake slip from the southern and central San Andreas fault with observed slip events at the Wrightwood paleoseismic site [*Weldon et al.*, 2004]. Wrightwood slip observations were tallied in 1-m bins and plotted by mean frequency (blue squares). Modeled earthquake slip was plotted by stress recovery time from Figure 5a (red dots). Modeled earthquake frequency is consistent with observed provided they are compared as in Figure 11a. (b)Wrightwood slip events viewed in time sequence. It is clear that they are not time-predictable because event timing does not seem related to preceding event slip magnitudes. Thus, while frequency of like slip events can be related to stress drop, there appears to have been enough stress on the San Andreas fault to sustain earthquake clustering. (c) Example of overlapping earthquakes, which might be an alternative explanation. However, by analysis of other San Andreas paleoseismic sites, *Weldon et al.* [2005] showed that earthquake overlap cannot explain all observed clustered slip events.

ing repeats of a particular earthquake size, and are not consistent with the observations in sequence. For example, the stress-based model calculates a ~550-year waiting period (Figure 5a) following a $M$ = 7.8 event on the central San Andreas fault. However, observations at Wrightwood [*Weldon et al.*, 2004] showed that $M \geq 7.0$ earthquakes frequently occurred after 100-year waiting times (Figure 11b). On average though, a ~550-year waiting period would be applicable between two $M$ = 7.8 events (Figure 11a). In other words, there may be multiple earthquake sizes that characterize the same fault segment.

[27] Use of inferred recurrence estimates in a time-dependent probability calculation for the San Andreas fault may require careful consideration of magnitude since it appears slip from previous earthquakes does not necessarily reset stress on the fault. If there is a set of known characteristic events on a fault segment, then it appears their frequencies, whether modeled or observed, should be treated independently. In the absence of detailed paleoseis-

mic observations, Gutenber-Richter extrapolations for large earthquake rates from smaller shocks are permissible from a stress balance perspective.

## 4. Conclusions

[28] I produced a set of $M \geq 7.0$ earthquake recurrence intervals for three San Andreas fault sections from the ratio of calculated static stress drop to geodetically derived secular stressing rate (Figure 5). Calculations showed that stress drop and recovery are expected to affect volumes of crust surrounding the earthquake with recovery times decreasing with distance away from the model ruptures (Figures 3, 7, and 9). Postseismic viscoelastic relaxation and afterslip were calculated to have significant impact on recurrence times (up to 25% reduction) for $M \geq 7.6$ earthquakes. Regional differences were noted, with the northern San Andreas section showing slightly shorter recurrence times as compared with more southerly sections, a result of higher rate, more concentrated stressing in the north. In each region, the array of calculated $M \geq 7.0$ earthquake frequencies could be fit to a Gutenberg-Richter relation that was consistent with the intercepts and slopes (a and b values) of observed $M \leq 6.0$ regional seismicity. Slip required to generate simulated earthquakes in the model and their calculated frequencies were shown to be consistent with the frequencies of observed slip events at the Wrightwood paleoseismic site [*Weldon et al.*, 2004]. The Wrightwood sequence is inconsistent with time predictability, where stress drop of the most recent earthquake divided by the stressing rate yields time to the next shock [*Shimazaki and Nakata*, 1980]. Modeling results from this study show that a Gutenberg-Richter distribution of $M \geq 7.0$ earthquakes balances San Andreas fault earthquake stress drop against tectonic stressing rates. Thus if evidence for large characteristic earthquakes on a given fault segment is lacking, a Gutenberg-Richter model is a viable alternative for hazard assessment.

[29] **Acknowledgments.** I thank the two referees, Yan Kagan, and one anonymous for their constructive suggestions. I also thank the editors and editorial staff for their time and effort with this manuscript.

## References

Anderson, E. M. (1951), *The Dynamics of Faulting and Dyke Formation*, 206 pp., Oliver and Boyd, Edinburgh.

Birch, F. (1966), Compressibility: Elastic constants, in *Handbook of Physical Constants*, edited by S. P. Clark Jr., *Mem.Geol. Soc. Am.*, *97*, 97–173.

Bürgmann, R., S. Ergintav, P. Segall, E. Hearn, S. McClusky, R. Reilinger, H. Woith, and J. Zschau (2002), Time-space variable afterslip on and deep below the Izmit earthquake rupture, *Bull. Seismol. Soc. Am.*, *92*, 126–137.

Caristan, Y. (1982), The transition from high temperature creep to fracture in Maryland diabase, *J. Geophys. Res.*, *87*, 6781–6790.

Carter, N. L., and M. C. Tsenn (1987), Flow properties of the lithosphere, *Tectonophysics*, *136*, 27–63.

Christensen, N. I. (1996), Poisson's ratio and crustal seismology, *J. Geophys. Res.*, *101*, 3139–3156.

Christensen, N. I., and W. D. Mooney (1995), Seismic velocity structure and composition of the continental crust: A global view, *J. Geophys. Res.*, *100*, 9761–9788.

Ellsworth, W. L. (2003), Appendix D: Magnitude and area data for strike-slip earthquakes: Earthquake probabilities in the San Francisco Bay region: 2002 to 2031, *U. S. Geol. Surv. Open File Rep., 03-214*.

Felzer, K. R., and E. E. Brodsky (2005), Testing the stress shadow hypothesis, *J. Geophys. Res.*, *110*, B05S09, doi:10.1029/2004JB003277.

Freed, A. M., and R. Bürgmann (2004), Evidence of powerlaw flow in the Mojave desert mantle, *Nature*, *430*, 548–551, doi:10.1038/nature02784.

Freed, A. M., and J. Lin (1998), Time-dependent changes in failure stress following thrust earthquakes, *J. Geophys. Res.*, *103*, 24,393–24,409.

Hansen, F. D., and N. L. Carter (1983), Semibrittle creep of dry and wet Westerly granite at 1000 MPa, *Proc. U.S. Symp. Rock Mech.*, *24th*, 429–447.

Harris, R. A., and R. W. Simpson (1996), In the shadow of 1857: The effect of the great Ft. Tejon earthquake on subsequent earthquakes in southern California, *Geophys. Res. Lett.*, *23*, 229–232.

Harris, R. A., and R. W. Simpson (1998), Suppression of large earthquakes by stress shadows: A comparison of Coulomb and rate-and-state failure, *J. Geophys. Res.*, *103*, 24,439–24,452.

Hearn, E. H., R. Bürgmann, and R. E. Reilinger (2002), Dynamics of Izmit earthquake postseismic deformation and loading of the Düzce earthquake hypocenter, *Bull. Seismol. Soc. Am.*, *92*, 172–193.

Kagan, Y. Y., and D. D. Jackson (1999), Worldwide doublets of large shallow earthquakes, *Bull. Seismol. Soc. Am.*, *89*, 1147–1155.

Kenner, S., and P. Segall (1999), Time-dependence of the stress shadowing effect and its relation to the structure of the lower crust, *Geology*, *27*, 119–122.

Kirby, S. H., and A. K. Kronenberg (1987), Rheology of the lithosphere: Selected topics, *Rev. Geophys.*, *25*, 1219–1244.

Li, Q., and M. Liu (2006), Geometrical impact of the San Andreas Fault on stress and seismicity in California, *Geophys. Res. Lett.*, *33*, L08302, doi:10.1029/2005GL025661.

Lisowski, M., J. C. Savage, and W. H. Prescott (1991), The velocity field along the San Andreas fault in central and southern California, *J. Geophys. Res.*, *96*, 8369–8389.

Michael, A. J. (2005), Viscoelasticity, postseismic slip, fault interactions, and the recurrence of large earthquakes, *Bull. Seismol. Soc. Am.*, *95*, 1594–1603.

Murray, J., and P. Segall (2002), Testing time-predictable earthquake recurrence by direct measurement of strain accumulation and release, *Nature*, *419*, 287–291.

Nostro, C., A. Piersanti, and M. Cocco (2001), Normal fault interaction caused by coseismic and postseismic stress changes, *J. Geophys. Res.*, *106*, 19,391–19,410.

Nur, A., and G. Mavko (1974), Postseismic viscoelastic rebound, *Science*, *183*, 204–206.

Parsons, T. (2002), Post-1906 stress recovery of the San Andreas fault system calculated from three-dimensional finite element analysis, *J. Geophys. Res.*, *107*(B8), 2162, doi:10.1029/2001JB001051.

Parsons, T. (2006), Tectonic stressing in California modeled from GPS observations, *J. Geophys. Res.*, *111*, B03407, doi:10.1029/2005JB003946.

Pollitz, F. F. (2001), Viscoelastic shear zone model of a strike-slip earthquake cycle, *J. Geophys. Res.*, *106*, 26,541–26,560.

Pollitz, F. F., G. Peltzer, and R. Bürgmann (2000), Mobility of continental mantle: Evidence from postseismic geodetic observations following the 1992 Landers earthquake, *J. Geophys. Res.*, *105*, 8035–8054.

Savage, J. C. (1992), The uncertainty in earthquake conditional probabilities, *Geophys. Res. Lett.*, *19*, 709–712.

Savage, J. C., and W. H. Prescott (1978), Asthenospheric readjustment and the earthquake cycle, *J. Geophys. Res.*, *83*, 3369–3376.

Savage, J. C., J. L. Svarc, and W. H. Prescott (1999), Geodetic estimates of fault slip rates in the San Francisco Bay area, *J. Geophys. Res.*, *104*, 4995–5002.

Shimazaki, K., and T. Nakata (1980), Time-predictable recurrence model for large earthquakes, *Geophys. Res. Lett.*, *7*, 279–282.

Smith, B., and D. Sandwell (2003), Coulomb stress accumulation along the San Andreas Fault system, *J. Geophys. Res.*, *108*(B6), 2296, doi:10.1029/2002JB002136.

Smith, B., and D. Sandwell (2006), A model of the earthquake cycle along the San Andreas Fault system for the past 1000 years, *J. Geophys. Res.*, *111*, B01405, doi:10.1029/2005JB003703.

Stein, R. S. (1999), The role of stress transfer in earthquake occurrence, *Nature*, *402*, 605–609.

Stein, R. S., A. A. Barka, and J. H. Dieterich (1997), Progressive failure on the North Anatolian fault since 1939 by earthquake static stress triggering, *Geophys. J. Int.*, *128*, 594–604.

Weldon, R., K. Scharer, T. Fumal, and G. Biasi (2004), Wrightwood and the earthquake cycle: What the long recurrence record tells us about how faults work, *GSA Today*, *14*, 4–10, doi:10.1130/1052-5173(2004)014.

Weldon, R. J., T. E. Fumal, G. P. Biasi, and K. M. Scharer (2005), Past and future earthquakes on the San Andreas Fault, *Science*, *308*, 966–967.

Wells, D. L., and K. J. Coppersmith (1994), New empirical relationships among magnitude, rupture length, rupture width, rupture area, and surface displacement, *Bull. Seismol. Soc. Am.*, *84*, 974–1002.

Working Group on California Earthquake Probabilities (1995), Seismic hazards in Southern California: Probable earthquakes, 1994 to 2024, *Bull. Seismol. Soc. Am.*, *85*, 379–439.

Working Group on California Earthquake Probabilities (2003), Earthquake probabilities in the San Francisco Bay region: 2002 to 2031, *U.S. Geol. Surv. Open File Rep., 03-214*.

T. Parsons, U.S. Geological Survey, 345 Middlefield Road, MS 999, Menlo Park, CA 94025, USA. (tparsons@usgs.gov)